ChemPubSoc Europe

DOI: 10.1002/cssc.201801480

CHEMSUSCHEM Full Papers

Tuning Cobalt and Nitrogen Co-Doped Carbon to Maximize Catalytic Sites on a Superabsorbent Resin for Efficient Oxygen Reduction

Mengran Liu,[a] Hai Lin,[a] Zongwei Mei,[a] Jinlong Yang,[a] Jie Lin,[b] Yidong Liu,*[a] and Feng Pan*[a]

The electrocatalytic performance and cost of oxygen reduction reaction (ORR) catalysts are crucial to many renewable energy conversion and storage systems/devices. Recently, transition-metal/nitrogen-doping carbon catalysts (M–N–C) have attracted tremendous attention due to their low cost and excellent catalytic activities; however, they are restricted in large-scale commercial applications by complex preparation processing. Here, a facile strategy to prepare Co–N–C catalysts has been developed. A kind of superabsorbent resin normally found in diapers, poly(acrylic acid-acrylamide), is used to adsorb a transition-metal cobalt salt and a pyrolysis strategy at 800 °C under an argon atmosphere is followed. The resin simultaneously plays a multiple role, which includes structural support, dispersing cobalt ions by coordinate bonds, and providing a carbon and nitrogen source. Attributed to the conductive carbon frameworks and abundant catalytic sites, the Co–N–C catalyst exhibits an excellent electrocatalytic performance. High onset potential (0.96 V vs. reversible hydrogen electrode, RHE), half-wave potential (0.80 V vs. RHE), and a large diffusion-limited current density (4.65 mA cm^{-2}) are achieved for the ORR, which are comparable or superior to the commercial 20% Pt/C and reported M–N–C ORR electrocatalysts. This work provides a universal dispersion technology for Co–N–C catalyst, which makes it a very promising candidate toward the ORR.

Introduction

The oxygen reduction reaction (ORR) is a critically important reaction in many renewable energy conversion and storage systems/devices, such as fuel cells, metal/air batteries,[1] and some industrial processes, such as the chloralkali electrolysis.[2] Nevertheless, due to the inherently sluggish kinetics of the ORR compared with that of the anodic reaction, it dramatically limits the energy conversion efficiency and turns out to be the bottleneck to develop these energy devices.[3] Currently, the state-of-the-art catalysts for ORR are still noble-metal catalysts, especially platinum (Pt) catalysts owing to their low overpotentials and large current densities.[3a] However, these noble-metal catalysts suffer from low earth reserves, high cost, poisoning effects, and insufficient stability that severely limits their large-scale commercialization.[4] In view of this, extensive research efforts have been carried out to overcome these problems, including the synthesis of noble-metal/transition-metal (such as Fe, Co, Cu, and Ni) alloys with special structural control[4a,5] and entirely new non-noble-metal materials doped with the active elements, such as metal-free heteroatom-doped carbon materials,[1c,6] transition-metal/nitrogen-doping carbon materials (M–N_x–C),[7] transition-metal nitrides,[8] oxides,[9] and sulfides,[10] as well as their hybrids,[7b,11] etc. Generally, there are a series of techniques to prepare the above catalysts which are mainly divided into two aspects.[12] The major one is the thermal treatment strategy of precursors with the help of a sol–gel technique,[13] the template method,[14] and in situ synthesis[15] . The second aspect focuses on new strategies, involving chemical vapor deposition,[16] the wet-chemical strategy,[17] microwave methods,[18] etc. Among these new catalyst types, the M–N_x–C (M = Fe and/or Co) catalysts are believed to be the most recent promising candidates for cathode catalysts.[19] In particular, carbon materials with high electron conductivity, excellent corrosion resistance, and tunable surface properties make them good supporters for active sites.[3a,20] Normally, The M–N_x–C catalysts are synthesized by thermal treatment of precursors at certain temperatures in an inert environment (nitrogen or argon).[21] Upon pyrolysis, structure and morphology get changed and active sites for ORR are formed. Although the catalytic mechanism of this kind of catalysts is still under debate, the formation of the ORR active sites strongly depends on the composition of the precursor.[19] In 1964, Jasinski reported that cobalt phthalocyanine could work in catalyzing the ORR[22] and a lot of N-containing precursors with transition metals have been studied, which contain phthalocyanine,[23] porphyrin,[24] corrole,[25] polyacrylonitrile,[26] polypyrrole,[27] polyaniline,[28] and polymerizable ionic liquid[29] etc. Among these N-containing precursors, it is particularly difficult and complex

[a] M. Liu, H. Lin, Dr. Z. Mei, J. Yang, Prof. Y. Liu, Prof. F. Pan
School of Advanced Materials
Peking University Shenzhen Graduate School
Shenzhen 518055 (P.R. China)
E-mail: liuyd@pkusz.edu.cn
panfeng@pkusz.edu.cn

[b] J. Lin
Fujian Institute of Subtropical Botany
Xiamen 361006 (P.R. China)

Supporting Information and the ORCID identification number(s) for the author(s) of this article can be found under: https://doi.org/10.1002/cssc.201801480.

for the regulation of nitrogen content and the formation of nitrogen-functional active groups with metal and carbon atoms.

Here, we report a one-step synthesis (Scheme 1) and pyrolysis method to prepare Co–N_x–C catalysts. By using the inexpensive superabsorbent resin poly(acrylic acid-acrylamide) [poly(AA-AM)] to absorb cobalt salt solution [Co^{2+}@poly(AA-AM)], the aims of a high-level spontaneous dispersion, structural support without additional template, and easy doping were achieved in one step. Pyrolysis of as-prepared Co^{2+}@poly(AA-AM) was carried out at 800 °C under an argon atmosphere. PAA-AM not only plays a role in providing ligands, but also helps in achieving structural support easily because of the existence of cross-linked networks. On the other hand, due to the presence of amino and carboxyl groups, the transition-metal ions are selectable, and the ratio of acrylic and acrylamide monomers can also be used to regulate the nitrogen content of the precursor. Although there are no pyridinium moieties and ring-forming structure on the PAA-AM molecule chain, it can be self-assembled with transition-metal ions. After pyrolysis, it was confirmed that pyridinic N was formed to achieve excellent electrocatalytic performances. The obtained Co–N–C catalysts show flake morphology with a high surface area of ≈500 $m^2 g^{-1}$, uniform distribution of Co–N species, and a certain nitrogen-doping content in a continuous carbon framework. Our Co–N–C catalysts display superior ORR performances but with an extremely low cost compared to most other ORR electrocatalysts, with a positive half-wave potential of 0.80 V versus the reversible hydrogen electrode (RHE). As a whole, the ratio of the N atom in the precursors used in our work is the smallest compared with previous studies, but the catalytic performance is equal to or better than the other works. This shows that the utilization of nitrogen atoms is higher and a high proportion of doping can be achieved.

Scheme 1. Illustration of the preparation procedure and ORR process of the Co–N–C catalyst.

Results and Discussion

FTIR spectra of pure hydrogels poly(AA-AM) and Co^{2+}@poly(AA-AM) are presented in Figure 1a. Several distinct characteristic absorption peaks can be clearly identified from the spectrum of pure hydrogels, confirming the copolymerization of AA and AM. In particular, the two peaks located at 1650 cm^{-1} (the absorption peak of the carbonyl group C=O connected to the amide group $-CONH_2$) and 1546 cm^{-1} (carbonyl group antisymmetric stretching vibration peak of $-COO^-$), respectively, suggest the existence of the amido groups and the carboxylic groups in the crosslinking network, which are hydrophilic groups. When hydrogels were added to the cobalt acetate solution, those ionizable groups on the network chain ionized in solution; as a consequence, the positive ions existed in free-form, whereas the negative ions were still connected with the network chain. These similarly charged adjacent groups repelled each other, and then the network expanded, providing space for water molecules and cobalt ions to freely access the crosslinking network. The two characteristic peaks mentioned above of Co^{2+}@poly(AA-AM) shifted towards lower wavenumbers, about 30 cm^{-1}, compared with those of pure hydrogel poly(AA-AM). This is due to ionic bonds formed between Co^{2+} and the $-COO^-$ group, which formed a stable complexing structure with $-CONH_2$, which promoted the uniform distribution and stability of cobalt ions in the hydrogels. In this work, hydrogels serving as a superb template that contains the $-COO^-$ and $-CONH_2$ groups plays a significant role in providing structural support and prompting cobalt ion dispersion.

The pyrolysis of as-prepared Co^{2+}@poly(AA-AM) was performed at high temperature in an inert atmosphere to complete the transformation of the organic to inorganic phase. The TGA/DSC tests were carried out to study the thermal decomposition performance of Co^{2+}@poly(AA-AM). At low temperature, moisture in the sample volatilized gradually. As the temperature rose, the organic groups and other small molecules were heated and decomposed violently in the inert atmosphere. When the temperature had risen above the carbonization temperature, the noncarbon atoms were gradually eliminated, and the carbon atoms were further enriched and crosslinked. As the DSC curve of the Co^{2+}@poly(AA-AM) complex depicts (Figure S1, Supporting Information), an endothermic peak was observed at about 750 °C, which might be a result of the formation of a carbonaceous framework.[14b]

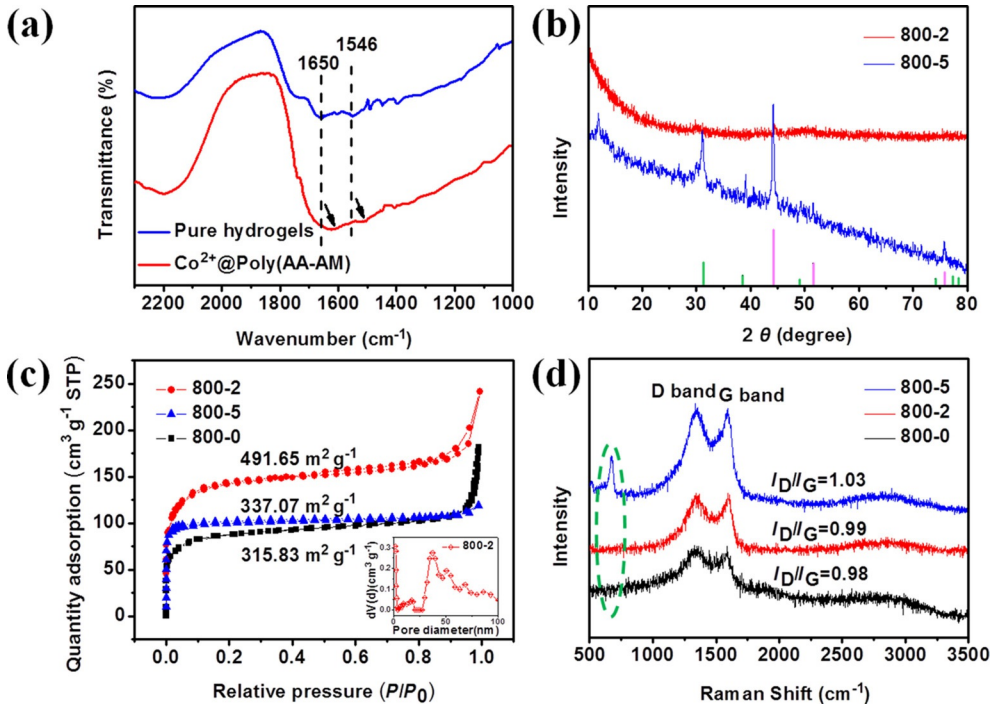

Figure 1. a) FTIR spectra of pure hydrogels poly(AA-AM) and Co^{2+}@poly(AA-AM). b) XRD patterns of 800-2 and 800-5 Co–N–C catalysts. c) Nitrogen adsorption–desorption isotherms and d) Raman spectra of 800-0, 800-2, and 800-5 Co–N–C catalysts; the inset of (c) shows the pore-size distribution of 800-2 Co–N–C catalysts.

Overall, the high ORR catalytic performance is in close connection with the surface properties, the elemental composition, and the interaction of the catalysts, for instance, a high active-site density, a proper porosity to facilitate mass transport, and a high degree of carbonization to achieve high electrical conductivity are essential parameters.[30]

XRD patterns of 800-2 and 800-5 Co–N–C catalysts are displayed in Figure 1b. No characteristic peak was observed in the XRD pattern of 800-2 Co–N–C, which might result from the formation of amorphous structures or small crystal grains. However, with the increase of cobalt content, the crystal structure of Co–N–C catalysts was changed. The diffraction peaks at 44.2, 51.5, and 75.9° are attributed to the (111), (200), and (220) planes of metallic Co (PDF#15-0806), respectively. Besides, the characteristic peaks at 31.3 and 38.6° are ascribed to the (220) and (222) plane of the Co_3O_4 phase (PDF#43-1003), implying the formation of Co–O moieties. From the results, we suspect that during the pyrolysis process, cobalt atoms congregate first to form metal nanoclusters, and then the rising cobalt content leads to the increasing size of the crystal; in the meantime, oxygen atoms may participate in the further formation of the Co–O structure.

SEM and TEM images are acquired to investigate the morphologies and microstructures of the catalysts. After the pyrolysis treatment and ball milling, a highly carbonized carbonaceous layer stacked up with particles and displaying an open porous structure was formed. These particles have a diameter range from about 100 nm to 2 μm (Figure 2a,b). To take further insights into the surface area and porosity of the catalysts,

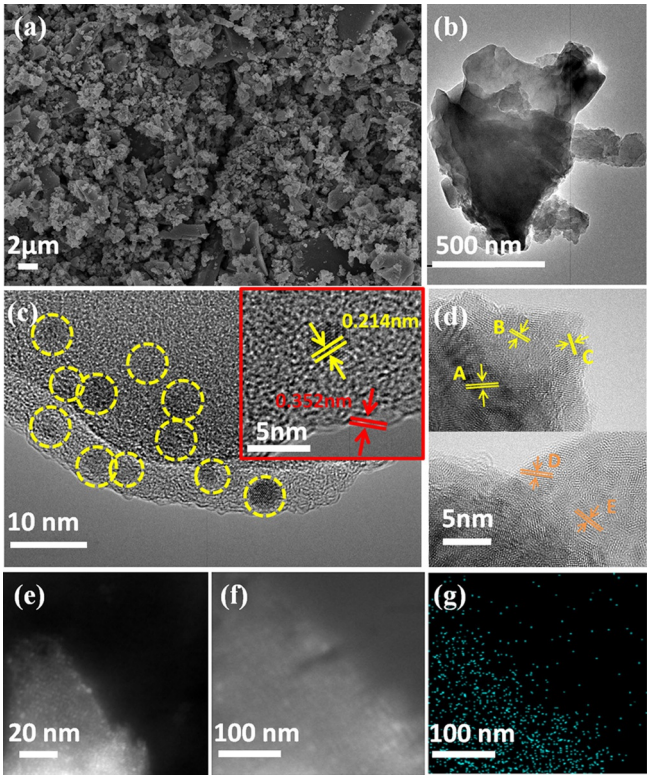

Figure 2. a) SEM image and b) TEM image of 800-2 Co–N–C catalyst. HR-TEM images of 800-2 Co–N–C catalyst (c) and 800-5 Co–N–C catalyst (d). e) HAADF-STEM image of 800-2 Co–N–C catalyst and the corresponding elemental mapping for element Co (g) of a part of this region (f).

N_2 sorption isotherms of 800-0, 800-2, and 800-5 Co–N–C catalysts were characterized (Figure 1c). All samples exhibited sharp uptakes at relatively low N_2 partial pressures (<0.01) indicating the existence of micropores (<2 nm),[26] whereas 800-2 Co–N–C also showed a well-defined hysteresis loop at higher N_2 pressures (from 0.4 to 1.0), which was classed as a typical type IV isotherm, suggesting the existence of mesopores as well.[9] The BET specific surface areas show an increase from 315.83 to 496.85 $m^2 g^{-1}$. The largest surface area and porosity of 800-2 probably attributes to the well-distributed cobalt element, which plays a catalytic part in carbonization and the formation of N–C doping.

HR-TEM of 800-2 Co–N–C (Figure 2c) shows that small nanoclusters (observed easily in the edge area and marked by yellow circles) with a narrow size distribution of about 2–5 nm were embedded in the carbon support uniformly.[14b] From the magnified insert in Figure 2c, it can be seen that these nanoclusters show a lattice spacing of 0.214 nm, which is slightly larger than the standard value of the (111) plane of metallic Co. We speculated that the larger lattice space may result from the intercalation of nitrogen, oxygen, and/or carbon into the cobalt spaces.[31] The carbonaceous fringes with a d-spacing of 0.352 nm correspond to the (002) plane of graphitic carbon. Figure 2d shows the HR-TEM image of 800-5 Co–N–C. The lattice spacing marked with A, B, and C in this figure is 0.208, 0.176, and 0.125 nm, corresponding to the (111), (200), and (220) crystal face of metallic cobalt, respectively; however, the grain size is much larger than that in 800-2. Besides, the lattice spacing presented by D and E is 0.243 and 0.286 nm, corresponding to the (220) (222) plane of Co_3O_4 respectively. The above information obtained from HRTEM images is consistent with XRD patterns. To further investigate the elemental distribution of Co in the catalyst, HAADF-STEM (Figure 2e) and HAADF-STEM-EDS mappings (Figure 2g) of 800-2 Co–N–C were conducted. As displayed in Figure 2e, the bright dots with relative light contrast correspond to Co atoms, whereas the dark contrast corresponds to carbonized support materials. From HAADF-STEM-EDS mappings of the edge area (Figure 2g and Figure S2, Supporting Information), the catalysts are mainly composed of C, O, N, and Co elements. The major elements C and N are evenly distributed, whereas the distributions of O and Co elements with relatively low proportions are clearly correlated and interactive, indicating that O atoms and nitrogen-doped carbon fragments are probably wrapped around the Co-containing structure.

The surface chemical composition and state of Co–N–C were further characterized by XPS as are shown in Figure 3. The survey spectrum (shown in Figure 3a and detailed parameters in Tables S1 and S2, Supporting Information) reconfirms the presence of C, N, O, and Co elements contained in Co–N–C catalysts. When the pyrolysis temperature rose from 700 to 800 °C, these catalysts showed an increase in C atomic content, but a decrease in N and O content, and almost invariant Co atomic content. When the temperature rose further to 900 °C, the sharp decrease in cobalt content may be due to the fact that cobalt atoms are congregated together and became blocked by surface carbon shells; therefore, some Co atoms cannot be detected by XPS. Simultaneously, the C atomic content still presents a trend of a slight increase. The results show that a higher carbonization degree is obtained at higher tem-

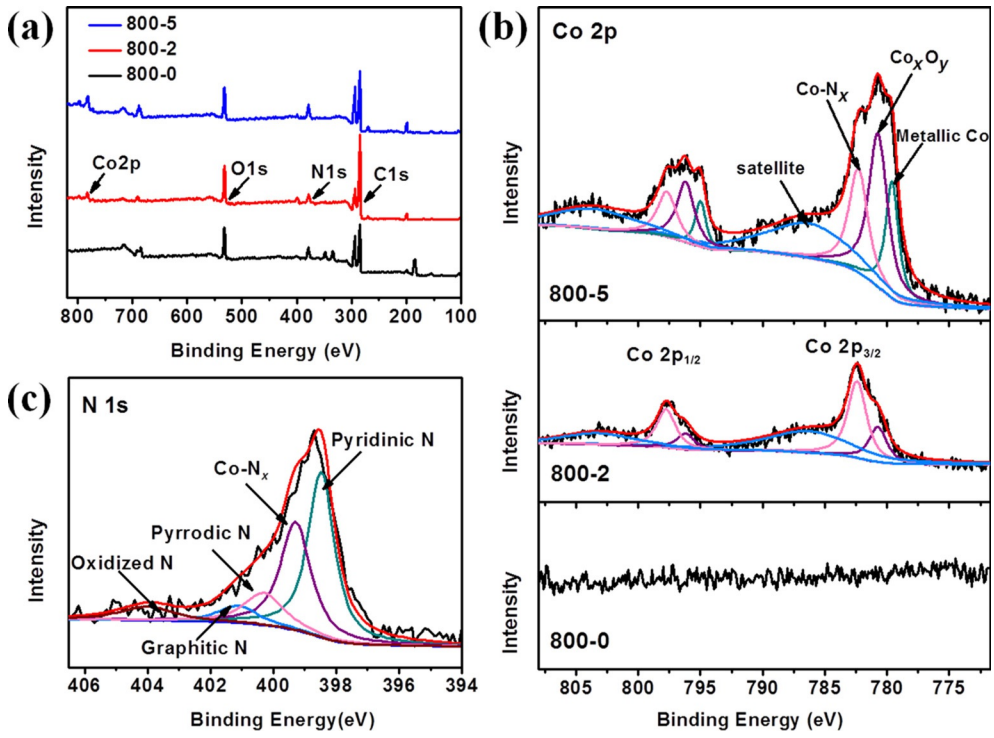

Figure 3. a) XPS spectra of 800-0, 800-2, and 800-5 Co–N–C catalysts. HR-XPS spectra of the Co 2p of 800-0, 800-2, and 800-5 Co–N–C catalysts (b) and the N 1s of 800-2 Co–N–C catalyst (c).

perature, which further improves the electrical conductivity of these catalysts.[12]

The high-resolution C 1s spectra (Figure S3, Supporting Information) of the catalysts are deconvoluted into five peaks, indicating the presence of different carbon species: C=C (284.43 eV), C–C (284.88 eV), C=O/C–N (286.20 eV), C–O/C=N (288.10 eV), and π–π (289.50 eV). The dominant carbon species of the 800-2 Co–N–C is C=C bonding in sp^2 hybridization (284.43 eV), whereas at the higher binding energy, 286.20 and 288.10 eV, carbon atoms are bound to more electronegative heteroatoms. As a result, the electron density of these carbon atoms is lower. The formed C^+ is believed to promote dissociative adsorption of oxygen, leading to a four-electron reduction pathway of ORR.[6] Overall, when the pyrolysis temperature increases, the percentages of C=C bonds increases as well, whereas C=O/C–N shows a decrease, indicating a higher carbonization (the detailed parameters are shown in Table S3, Supporting Information). Besides, there is no clear peak corresponding to a carbon atom bound to a Co atom, implying the absence or low content of cobalt carbide species, which is in good agreement with the XRD and the later Co 2p analysis results.

The formation of the Co–N bonds can be confirmed by the fitted high-resolution N 1s XPS spectra with an asymmetrical shape, as shown in Figure 3c. There are mainly three types of the nitrogen species: pyrrolic N (400.1 eV), metal-coordinated Co–N_x (399.2 eV), and pyridinic N (398.5 eV). Pyridinc N exists at the edge of graphite plans, and the nitrogen atom bonds to two carbon atoms, containing a lone electron pair, which can improve the electron donor or basic capacities of the carbon materials. Thereby, it can effectively improve the adsorption capacity of O_2 and onset potential for the ORR.[32] Besides, a weak but significant contribution at a high binding energy value of more than 401 eV (401.2 eV for graphitic N, and 404 eV for oxidized N) indicates that there are seldom nitrogen atoms that truly replace the carbon atoms in graphene-sheet binding conditions or band to O atoms directly, ascribed to polymer precursor poly(AA-AM). From the fitted high-resolution N 1s XPS spectra of 800-(0/5) Co–N–C (Figure S4, Supporting Information), with the addition of cobalt content, the main peak gradually shifted to a low binding energy, implying the increase of the percentage of pyridinic N in the total amount of N species. Recent studies reported that both pyridinic nitrogen and Co–N*x* were found to have ORR catalytic activity. Therefore, the enhanced catalytic activity for the ORR observed on the Co–N–C catalyst should be attributed to the formation of the pyridinic nitrogen and Co–N*x* in the process of high-temperature pyrolysis.[33]

High-resolution Co 2p spectra consist of Co 2p1/2, Co $2p_{3/2}$ and their corresponding satellites. Overall, these two main peaks of 800-2 Co–N–C catalyst (797.50 eV for Co $2p_{1/2}$ and 782.30 eV for Co $2p_{3/2}$) are separated by 15.2 eV, suggesting the mixed valence state of Co. Compared to 800-2, the two peaks of Co $2p_{1/2}$ and Co $2p_{3/2}$ of 700-2 Co–N–C are separated by 15 eV, confirming the only valence state (Figure S5, Supporting Information). As the cobalt content increases, the peak intensity of the Co 2p spectra increases, and the peak position gradually shifts toward the lower binding energy. In detail, the high-resolution Co $2p_{3/2}$ spectra of 800-5 Co–N–C catalyst is deconvoluted into three sharp peaks at about 779.59, 780.72, and 782.30 eV, attributed to metallic Co, Co_xO_y, and Co-N_x, respectively. Compared to 800-5, the absence of a metallic Co peak at 779.59 eV of 800-2 suggests that no or little inactive Co aggregates are formed. Furthermore, the largest percentage based on peak areas of Co–N_x species is observed at 800-2, which is considered to be one of the most effective catalytic sites for ORR.

Raman spectra of the catalysts are shown in Figure 1d and Figure S7, Supporting Information. There are two strong peaks at 1350 and 1597 cm^{-1}.These two peaks are assigned to the D (1350 cm^{-1}) and G band (1597 cm^{-1}) of carbon, as the D band is relative to the disorder and bonding between the heteroatom and carbon, whereas the G band arises from the in-plane vibration of the sp^2 carbon network.[3a] The ratio of the D and G band I_D/I_G is generally adopted to detect the graphitization and disorder of carbon materials. The I_D/I_G of catalysts Co–N–C-800 increase with the addition of cobalt from 0.98 to 1.03 (Figure 1d), implying the higher disordered and richer defects in the carbon matrix of the catalysts with a higher cobalt content. The results are fully consistent with the XPS findings. Moreover, the I_D/I_G of catalysts 700/800/900-2 Co–N–C decreases from 1.04 to 0.98 (Figure S7, Supporting Information) while the pyrolysis temperature increases, which indicates that a higher pyrolysis temperature can contribute to a higher graphitization degree. Moreover, a small peak located at 672 cm^{-1} demonstrates the existence of Co_3O_4,[34] which is consistent with the results of XRD and HR-TEM.

To investigate the electrocatalytic activity of the as-prepared catalysts, CV measurements were first conducted at 10 mV s^{-1} in N_2 or O_2-saturated 0.1 M KOH electrolytes. Compared to the result that no significant response occurs in N_2-saturated solutions, a well-defined cathodic peak near 0.80 V versus RHE was observed in O_2-saturated electrolytes, implying an effective ORR electrocatalytic activity of Co–N–C catalysts (Figure 4a). Furthermore, the LSV curves of 800-(0-5) Co–N–C are depicted in Figure 4b and the ORR performance parameters of catalysts are displayed in Table 1. Overall, the catalysts with relatively low cobalt doping exhibited better ORR activity with a similar positive onset potential of around 0.96 V (800-1, 800-2, 800-3) and a half-wave potential $E_{1/2}$ (potential corresponding to 50% of the diffusion-limited current density (j_L) in this work) of 0.80 V (800-1, 800-2). In particular, the most positive E_{onset} (corresponding to 5% of j_L) and the most positive $E_{1/2}$ of Co–N–C catalysts were 30 mV less and only 60 mV less than those of commercial 20% Pt/C, respectively. Moreover, those parameter values exceed some M–N–C catalysts or other kinds of catalysts with much higher costs reported in the literature (as shown in Tables S4–S7, Supporting Information). The obtained diffusion-limited current density of the 800-2 Co–N–C catalyst is 4.65 mA cm^{-2}, even larger than that of the commercial 20% Pt/C (4.64 mA cm^{-2}).

The 800-0 Co–N–C catalyst without any Co doping shows a relatively limited catalytic activity, thus the catalytic activity was promoted continuously alongside Co doping up to 2 wt%.

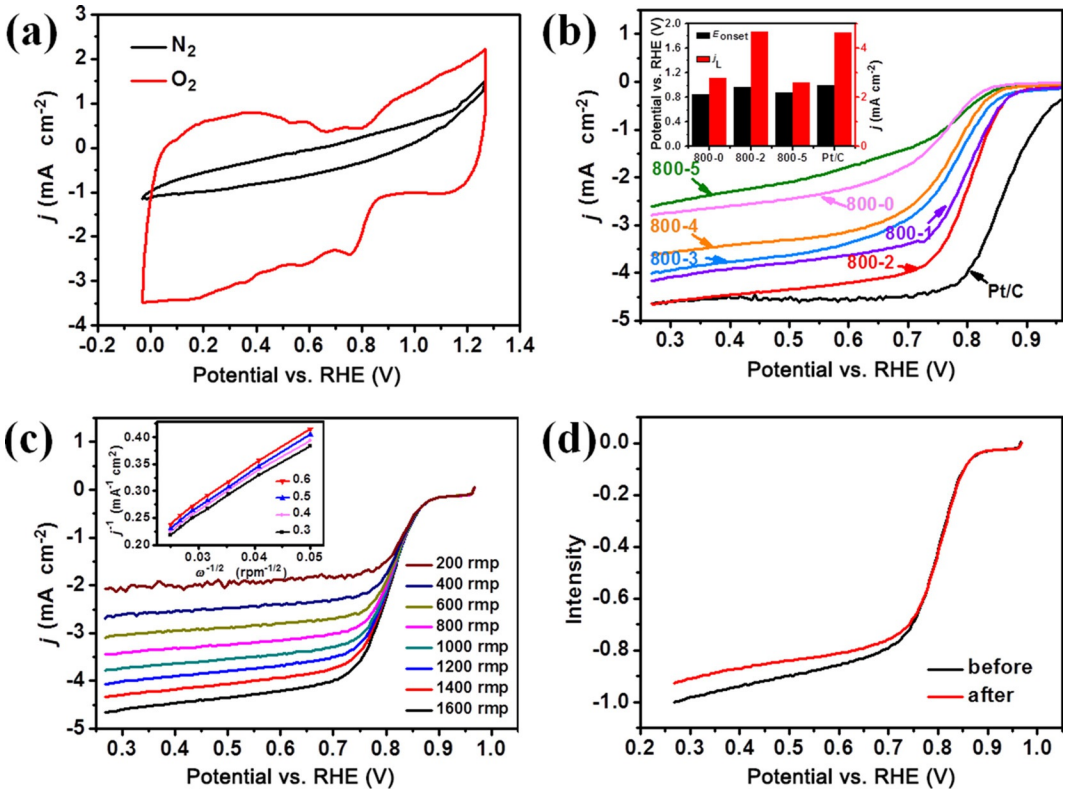

Figure 4. a) CV curves for 800-2 Co–N–C catalyst at a sweep rate of 10 mV s^{-1} in N_2 and O_2-saturated 0.1 M KOH electrolytes, respectively. b) LSV curves for 800-(0-5) Co–N–C catalysts at a sweep rate of 10 mV s^{-1} in an O_2-saturated 0.1 M KOH electrolyte. c) LSV curves for 800-2 Co–N–C catalyst at various rotation rates (values displayed in rpm) in an O_2-saturated 0.1 M KOH electrolyte; the inset of (c) shows the corresponding K–L plots derived from the RDE data. d) LSV curves of 800-2 Co–N–C catalyst before and after 2000 potential cycles, respectively.

Table 1. ORR electrocatalytic performance parameters of 800-(0–5) Co–N–C- from LSV in alkaline media.

Catalyst Co/*N*-C	E_{onset} vs. RHE [V]	$E_{1/2}$ vs. RHE [V]	Diffusion-limiting current [mA cm^{-2}]
800-0	0.85	0.74	2.79
800-1	0.95	0.80	4.17
800-2	0.96	0.80	4.65
800-3	0.96	0.76	4.01
800-4	0.88	0.76	3.63
800-5	0.87	0.76	2.61
Pt/C	0.99	0.86	4.64

An increased diffusion-limited current density and a positive-shifted half-wave potential $E_{1/2}$ can be observed. However, with further increasing of Co content, ORR catalytic activity of Co–N–C catalysts shows a trend of decreasing. Accurately, the effect of Co doping content on ORR catalytic activity is similar to a mountain plot as shown in the insert in Figure 4b, which is in good agreement with the above material characterization results. Combined with XPS analysis results, it can be concluded that Co–N species and pyridinic N plays a catalytic role in favoring the oxygen reduction reaction. When the cobalt content exceeds the optimized content, there will be a decrease in catalytic activity, which is attributed to the formation of inactive cobalt aggregation species, metal cobalt, and cobalt oxide, verified by XRD results. Moreover, increasing the cobalt content also increases the surface area and porosity, which is conducive to the exposure of metal-based active sites onto the surface, as well as the absorption and diffusion of molecular oxygen. Besides the percentages of Co elements, the pyrolysis temperature is one of the other critical synthesis parameters for the electrocatalysts. To further investigate the effect of pyrolysis temperature from 700 to 900 °C on ORR catalytic activity, the precursors were fixed at the optimum Co-doping content. Figure S8, Supporting Information, presents the LSV curves of 700/800/900-2 Co–N–C catalysts. Compared to 800-2 Co–N–C and 900-2 Co–N–C, the catalytic activity of 700-2 Co–N–C is negligible. According to the above analysis section, it is proved that there is no sign of the formation of Co–N bonds (Figure S5 and S6, Supporting Information). On the other hand, 700-2 Co–N–C is endowed with a slightly poor electric conductivity due to the existence of a certain amount of oxygen-contained groups and the halfway carbonization. When the temperature rises to 900 °C, the electrocatalysis performance of 900-2 Co–N–C catalyst would be affected by the removal of nitrogen elements.

To gain a deep understanding of the reaction kinetics and pathways, the polarization curves of 800-2 Co–N–C were measured at various rotating rates ranging from 200 to 1600 rpm, as shown in Figure 4c. The onset potentials remain constant while the current densities increase along with the increasing rotating rates, implying the kinetic-control of the ORR process. According to the Koutecky–Levich (K–L) equation, the corre-

sponding K–L plots under various potentials of 800-2 Co–N–C were obtained by transforming the RDE data. Clearly, all exhibit excellent linearity (see the inset of Figure 4c), suggesting the first-order reaction kinetics of the ORR toward the concentration of dissolved oxygen. As is known, the electrocatalytic reduction of O_2 in aqueous electrolytes goes through two generally recognized pathways, two-electron pathways or four-electron pathways.[30] The number of electrons n transferred per oxygen molecule was calculated to be about 3.89 based on the slope of the K–L plots, suggesting a near-four-electron oxygen reduction process. Furthermore, the durability of 800-2 Co–N–C was also measured. After 2000 continuous cycles (Figure 4d), no obvious changes occurred for $E_{1/2}$ and E_{onset}, whereas the diffusion-limited current density decreased a little by about 7%, implying the stability of the active site needed to be further improved. In addition, the ratio of AM/AA is a vital parameter of the superabsorbent resin that serves as a precursor for a nitrogen and carbon source in this work, which may also influence the electrocatalytic properties of the Co–N–C catalysts, which is, therefore, worth further study in our next work.

Based on the above experimental results, a possible mechanism was proposed to demonstrate the super catalytic activity of 800-2 Co–N–C catalyst. It is supposed that the pyridinic nitrogen and nitrogen-coordinated Co serve as catalytic active sites. On the one hand, a suitable pyrolysis temperature is mainly beneficial to guarantee a higher carbonization level and an optimal element proportion, especially as 800 °C is the minimum temperature to form nitrogen-coordinated Co. On the other hand, the appropriate introduction of Co not only offers nitrogen-coordinated Co active sites, but also contributes to promote the N-doping, porous structure, and specific surface area of the catalysts.[3a]

Conclusions

We have developed an effective dispersing technology using a superabsorbent resin that adsorbs metal ions followed by a pyrolysis strategy to fabricate Co–N–C-based catalysts for the oxygen reduction reaction (ORR). The resin provides the framework and doping element sources to coordinate with metal ions to form actives sites. In this work, poly(acrylic acid-acrylamide) (poly(AA-AM)) and cobalt were chosen to realize the idea. A large number of functional groups, amino and carboxyl, not only provide N and O, but also contribute to form nitrogen-doped carbon species and nitrogen-coordinated Co active sites. The Co–N–C catalyst exhibits an excellent electrocatalytic performance, which is comparable to the commercialized Pt/C catalyst, but the cost is far below it, which makes the composite catalyst easy to achieve commercialization instead of the Pt-based catalyst. In addition, the formula could be modified so that various resins and metal ions provide a large amount of possible couples, which makes the molecular-level dispersion technology universal and applicable to other related fields.

Experimental Section

Chemicals and reagents

Cobalt(II) acetate tetrahydrate ($C_4H_6O_4Co{\cdot}4H_2O$), methanol (MeOH), and KOH were purchased from National reagent (Shanghai, China). Isopropylalcohol [$(CH_3)_2CHOH$] was purchased from Fuyu reagent (Tianjin, China). Nafion solution (DuPont D520, 5%) and commercial Pt/C (20%) (Johnson Matthey catalysts) were used as a standard catalyst and was purchased from Hesen Company (Shanghai, China). All reagents were analytical grade and deionized water was used throughout this study.

Characterization

FTIR of poly(AA-AM) superabsorbent resin was verified by a Perkin–Elmer Frontier spectrophotometer. The thermogravimetry and differential scanning calorimetry (TGA/DSC) tests were measured using a TGA/DSC simultaneous thermal analyzer (TGA/DSC 1, Swiss Mettler Toledo). XRD patterns were carried on a X-ray diffractometer (D8 Advance, Bruker) using a silicon substrate without diffraction peak. The surface area and porosity of the Co–N–C catalysts were characterized by N_2 sorption isotherms using an accelerated surface area and porosimetry system (ASAP 2020 HD88, Micromeritics). Morphology and structure of the as-prepared Co–N–C were observed by the field-emission SEM (FESEM) (ZEISS SUPRA 55, Carl Zeiss, Germany). TEM images were obtained from the transmission electron microscope (JEM-3200FS, Japan). An energy-dispersive spectrometer (EDS) was used in the meantime. Raman spectra were recorded on an Raman microscope (iHR320, Horiba, Japan). XPS measurements were performed at an ESCALAB 250X X-ray photoelectron spectrometer (ESCALAB 250X, Thermo Fisher, England).

Electrode preparations

To prepare the catalyst dispersion for electrochemical analysis, powders (10 mg) were dispersed in a mixed solution containing Nafion solution (100 μL, 5 wt%), isopropyl alcohol (400 μL), and deionized water (1.5 mL). Subsequently, the mixed dispersion was sonicated for 20 min to form a homogeneous mixture. Finally, this mixture (10 μL) was dropped on a glassy carbon disk electrode (0.196 cm^2). After having dried at ambient temperature, the catalyst with a content of 0.25 mg cm^{-2} was loaded on the working electrode. As a comparison, a Pt/C (20 wt%) electrode was obtained by using a similar method. The loading content of Pt/C on the electrode and the test conditions are consistent with Co–N–C samples.

Electrochemical measurements

To investigate the ORR activities of the as-prepared catalysts, a series of electrochemical tests, including cyclic voltammetry (CV) and linear sweep voltammetry (LSV) were measured. All electrochemical measurements were performed on a SHANGHAI CHENHUA CHI760D/E electrocatalytic workstation attached to a rotating disk electrode (RDE). The whole testing process was executed in a normal three-electrode system at room temperature by choosing a glassy carbon electrode modified with various electrocatalysts as the working electrode, a Pt wire as the counter electrode, and an Ag/AgCl (in 3 M KCl solution) electrode as the reference electrode. Here, 0.1 M KOH aqueous solution was used as the electrolyte and deaerated by high purity O_2 or N_2 according to concrete conditions

throughout the testing process. CV experiments were recorded with a scan rate of 10 mV s^{-1}. LSV experiments were executed at 10 mV s^{-1} under rotating speeds varying from 200 to 1600 rpm. All potentials in this work were referred to the reversible hydrogen electrode (RHE), E (RHE) = E(Ag/AgCl) + 0.976 V.

Different publications give diverse definitions of the onset potential (E_{onset}) of ORR. It is defined as the potential value corresponding to 5% of the diffusion-limited current density (j_L) in this work.[2a] The mass activity was calculated by normalizing the kinetic-limiting current density (j_K) to the mass of active materials. The kinetics parameters were obtained from the mass-transport corrected polarization curve though the Levich–Koutechky equation [Eq. (1)]:

$$\frac{1}{j} = \frac{1}{j_L} + \frac{1}{j_k} = \frac{1}{j_k} + \frac{1}{B\omega^{1/2}} \quad (1)$$

in which j is the measured current density and j_k is the kinetic current density, respectively. ω is the electrode rotating rate. B is determined from the slope of the Koutechy–Levich (K–L) plots based on the Levich equation [Eq. (2)]:

$$B = 0.2nFC_0D_0^{2/3}\gamma^{-1/6} \quad (2)$$

For Equation (2), n is the number of electrons transferred per oxygen molecule, F the Faraday constant (96485 C mol^{-1}), C_0 the bulk concentration of O_2 (1.1×10^{-3} mol L^{-3}), D_0 the diffusion coefficient of O_2 in 0.1 M KOH (1.9×10^{-5} cm^2 s^{-1}), and γ the kinetic viscosity of the electrolyte (0.01 cm^2 s^{-1}).[7a] The constant 0.2 is adopted if the rotation rate is expressed in rpm.

Fabrication of the Co–N/C oxygen reduction reaction electrocatalyst

Synthesis of poly(AA-AM) superabsorbent resin

3D low cross-linking poly(AA-AM) was first prepared by radical polymerization with the aid of the coupling agent, *N*,*N*-methylene diacrylamide.[35] Throughout this work, the AA/AM ratio of poly(AA-AM) superabsorbent used in experiments was 7:3.

Synthesis of Co–N–C

Here, the synthesis process of cobalt, nitrogen-doped carbon materials Co–N–C is illustrated in Scheme 1. Firstly, cobalt ions were embedded in cross-linking poly(AA-AM) superabsorbent resin by easy adsorption. Several mg of cobalt(II) acetate $C_4H_6O_4{\cdot}Co{\cdot}4H_2O$ was dissolved in deionized water (10 mL). Then, as-prepared superabsorbent resin (0.5 g) was added into the above solution. The solid–liquid mixture was kept at room temperature for 1 h. The obtained products displayed a similar polyhedron shape but a different color (pink) to the pure hydrogels.

The prepared hybrid hydrogel was then frozen by liquid nitrogen and freeze-dried at −45 °C in a vacuum lyophilizer for 24 h. Subsequently, the dried mixture was calcined under an argon atmosphere in a tube furnace at a certain temperature for 2 h with a heating ramp of 5 °C min^{-1}, and then the furnace was cooled down to room temperature. After ball milling with ethanol for 8 h, the obtained products were purified by centrifugation and finally dried at 80 °C.

To study the effects of the pyrolysis temperature and the cobalt element content on the catalytic activities, seven kinds of Co–N–C catalysts were prepared by using the same method except for the difference of pyrolysis temperature or metal content. They were named as follows: 800-2 Co–N–C catalyst, in which "800" means the temperature of pyrolysis, and "2" represents the mass percentage of elemental cobalt in the as-prepared precursor solution and the resin.

Acknowledgements

This work was financially supported by the National Key R&D Program of China (2016YFB0700600), Shenzhen Science and Technology Research Grant (GJHZ20160229122304608).

Conflict of interest

The authors declare no conflict of interest.

Keywords: catalysts · cobalt · nitrogen · oxygen reduction reaction · superabsorbent resin

[1] a) A. Mahmood, W. Guo, H. Tabassum, R. Zou, *Adv. Energy Mater.* **2016**, *6*, 1600423; b) A. Shen, Y. Zou, Q. Wang, R. A. Dryfe, X. Huang, S. Dou, L. Dai, S. Wang, *Angew. Chem. Int. Ed.* **2014**, *53*, 10804 – 10808; *Angew. Chem.* **2014**, *126*, 10980 – 10984; c) I. T. Kim, M. J. Song, Y. B. Kim, M. W. Shin, *Int. J. Hydrogen Energy* **2016**, *41*, 22026 – 22033.

[2] a) W. Xia, A. Mahmood, Z. Liang, R. Zou, S. Guo, *Angew. Chem. Int. Ed.* **2016**, *55*, 2650 – 2676; *Angew. Chem.* **2016**, *128*, 2698 – 2726; b) J. Lee, B. Jeong, J. D. Ocon, *Curr. Appl. Phys.* **2013**, *13*, 309 – 321.

[3] a) M. Kuang, Q. Wang, P. Han, G. Zheng, *Adv. Energy Mater.* **2017**, *7*, 1700193; b) H.-X. Zhong, J. Wang, Y.-W. Zhang, W.-L. Xu, W. Xing, D. Xu, Y.-F. Zhang, X.-B. Zhang, *Angew. Chem. Int. Ed.* **2014**, *53*, 14235 – 14239; *Angew. Chem.* **2014**, *126*, 14459 – 14463; c) Y. Qiu, J. Huo, F. Jia, B. H. Shanks, W. Li, *J. Mater. Chem. A* **2016**, *4*, 83 – 95.

[4] a) Y. Zhou, K. Neyerlin, T. S. Olson, S. Pylypenko, J. Bult, H. N. Dinh, T. Gennett, Z. Shao, R. O'Hayre, *Energy Environ. Sci.* **2010**, *3*, 1437 – 1446; b) R. Zhang, Y. Li, L. Liu, M. Jiang, W. Wang, *Ionics* **2017**, *23*, 1849 – 1859.

[5] a) L. Wang, Z. Tang, W. Yan, Q. Wang, H. Yang, S. Chen, *J. Power Sources* **2017**, *343*, 458 – 466; b) T. Toda, H. Igarashi, H. Uchida, M. Watanabe, *J. Electrochem. Soc.* **1999**, *146*, 3750 – 3756; c) S. Liu, I. S. Amiinu, X. Liu, J. Zhang, M. Bao, T. Meng, S. Mu, *Chem. Eng. J.* **2018**, *342*, 163 – 170.

[6] L. Yang, S. Jiang, Y. Zhao, L. Zhu, S. Chen, X. Wang, Q. Wu, J. Ma, Y. Ma, Z. Hu, *Angew. Chem. Int. Ed.* **2011**, *50*, 7132 – 7135; *Angew. Chem.* **2011**, *123*, 7270 – 7273.

[7] a) J. Gao, N. Ma, Y. Zheng, J. Zhang, J. Gui, C. Guo, H. An, X. Tan, Z. Yin, D. Ma, *ChemCatChem* **2017**, *9*, 1601 – 1609; b) P. Subramanian, R. Mohan, A. Schechter, *ChemCatChem* **2017**, *9*, 1969 – 1978.

[8] Y. Dong, Y. Deng, J. Zeng, H. Song, S. Liao, *J. Mater. Chem. A* **2017**, *5*, 5829 – 5837.

[9] J. Chen, N. Zhou, H. Wang, Z. Peng, H. Li, Y. Tang, K. Liu, *Chem. Commun.* **2015**, *51*, 10123 – 10126.

[10] S. Dou, L. Tao, J. Huo, S. Wang, L. Dai, *Energy Environ. Sci.* **2016**, *9*, 1320 – 1326.

[11] a) Y. Tong, P. Chen, T. Zhou, K. Xu, W. Chu, C. Wu, Y. Xie, *Angew. Chem. Int. Ed.* **2017**, *56*, 7121 – 7125; *Angew. Chem.* **2017**, *129*, 7227 – 7231; b) C. H. Choi, M. W. Chung, S. H. Park, S. I. Woo, *Phys. Chem. Chem. Phys.* **2013**, *15*, 1802 – 1805.

[12] T. He, H. Xue, X. Wang, S. He, Y. Lei, Y. Zhang, R. Shen, Y. Zhang, J. Xiang, *Nanoscale* **2017**, *9*, 8341 – 8348.

[13] P. H. Matter, E. Wang, M. Arias, E. J. Biddinger, U. S. Ozkan, *J. Phys. Chem. B* **2006**, *110*, 18374 – 18384.

[14] a) X. Song, L. Guo, X. Liao, J. Liu, J. Sun, X. Li, *Small* **2017**, *13*, 1700238; b) H. Huang, Q. Wang, Q. Wei, Y. Huang, *Int. J. Hydrogen Energy* **2015**, *40*, 6072 – 6084.

[15] C. J. Shearer, A. Cherevan, D. Eder, *Adv. Mater.* **2014**, *26*, 2295 – 2318.

[16] D. S. Choi, A. W. Robertson, J. H. Warner, S. O. Kim, H. Kim, *Adv. Mater.* **2016**, *28*, 7115 – 7122.

[17] Z. S. Wu, S. Yang, Y. Sun, K. Parvez, X. Feng, K. Mullen, *J. Am. Chem. Soc.* **2012**, *134*, 9082 – 9085.
[18] U. B. Nasini, V. Gopal Bairi, S. Kumar Ramasahayam, S. E. Bourdo, T. Viswanathan, A. U. Shaikh, *ChemElectroChem* **2014**, *1*, 573 – 579.
[19] S. Chao, Q. Cui, Z. Bai, H. Yan, K. Wang, L. Yang, *Int. J. Hydrogen Energy* **2014**, *39*, 14768 – 14776.
[20] Y.-P. Zhu, Y. Liu, Y.-P. Liu, T.-Z. Ren, G.-H. Du, T. Chen, Z.-Y. Yuan, *J. Mater. Chem. A* **2015**, *3*, 11725 – 11729.
[21] S. Fu, C. Zhu, H. Li, D. Du, Y. Lin, *J. Mater. Chem. A* **2015**, *3*, 12718 – 12722.
[22] R. Jasinski, *Nature* **1964**, *201*, 1212 – 1213.
[23] a) L. Ding, J. Qiao, X. Dai, J. Zhang, J. Zhang, B. Tian, *Int. J. Hydrogen Energy* **2012**, *37*, 14103 – 14113; b) W. Li, A. Yu, D. C. Higgins, B. G. Llanos, Z. Chen, *J. Am. Chem. Soc.* **2010**, *132*, 17056 – 17058.
[24] M. Jahan, Q. Bao, K. P. Loh, *J. Am. Chem. Soc.* **2012**, *134*, 6707 – 6713.
[25] H.-C. Huang, I. Shown, S.-T. Chang, H.-C. Hsu, H.-Y. Du, M.-C. Kuo, K.-T. Wong, S.-F. Wang, C.-H. Wang, L.-C. Chen, K.-H. Chen, *Adv. Funct. Mater.* **2012**, *22*, 3500 – 3508.
[26] Y. Wang, J. Yang, R. Du, L. Chen, *ACS Appl. Mater. Interfaces* **2017**, *9*, 23731 – 23740.
[27] R. Bashyam, P. Zelenay, *Nature* **2006**, *443*, 63 – 66.
[28] G. Wu, K. L. More, C. M. Johnston, P. Zelenay, *Science* **2011**, *332*, 443 – 447.
[29] J. Gao, N. Ma, J. Zhai, T. Li, W. Qin, T. Zhang, Z. Yin, *Ind. Eng. Chem. Res.* **2015**, *54*, 7984 – 7989.
[30] J. Masa, W. Xia, M. Muhler, W. Schuhmann, *Angew. Chem. Int. Ed.* **2015**, *54*, 10102 – 10120; *Angew. Chem.* **2015**, *127*, 10240 – 10259.
[31] Y. Qian, Z. Liu, H. Zhang, P. Wu, C. Cai, *ACS Appl. Mater. Interfaces* **2016**, *8*, 32875 – 32886.
[32] J. Zhang, H. Zhou, X. Liu, J. Zhang, T. Peng, J. Yang, Y. Huang, S. Mu, *J. Mater. Chem. A* **2016**, *4*, 15870 – 15879.
[33] K. Lee, L. Zhang, H. Lui, R. Hui, Z. Shi, J. Zhang, *Electrochim. Acta* **2009**, *54*, 4704 – 4711.
[34] X. Liu, I. S. Amiinu, S. Liu, K. Cheng, S. Mu, *Nanoscale* **2016**, *8*, 13311 – 13320.
[35] H. Lin, *J. Wuyi Univ.* **2016**, *35*, 6 – 10.

Manuscript received: July 2, 2018
Revised manuscript received: August 9, 2018
Accepted manuscript online: August 23, 2018
Version of record online: September 24, 2018